3

Bimolecular Collision Dynamics of H_3^+ + CO Reaction

During the past several decades, numerous cationic, anionic, and neutral molecules containing few atoms to polycyclic aromatic hydrocarbons have been identified in the interstellar media and the chemistry of these species has received considerable attention in the literature[Smith, 1992; Herbst, 1995; Snow and Bierbaum, 2008; Kaiser *et al.*, 2015]. Ion-molecule reactions occurring in the interstellar media play an important role in determining the molecular abundances in space[Anicich, 1993; Larsson *et al.*, 2012]. The most widely distributed ionic species in space is the H_3^+ molecular ion[Oka, 1980; Herbst, 2000; Oka, 2012] which is highly reactive due to its tendency to lose a proton easily and is known to initiate several chemical reaction networks[Burt *et al.*, 1970; Kim *et al.*, 1975; Oka, 2006]. The proton transfer reaction between H_3^+ and another abundant molecule CO (shown in Figure 3.1) is particularly important, since the reaction products – the stable formyl cation (HCO^+) and the metastable isoformyl cation (HOC^+) – are precursors for several complex molecules found in space[Herbst, 2005]. Stability of formyl cation is due to the partial negative charge on the carbon atom in the CO molecule. These two ions initiate different reaction chains, and thus an understanding of their relative abundance in the interstellar environment is essential[Woods *et al.*, 1983; Ziurys and Apponi, 1995; Sternberg, 1995; Apponi and Ziurys, 1997; Savage and Ziurys, 2004; Liszt *et al.*, 2004; Fuente *et al.*, 2005]. There are many studies available in the literature on this subject wherein HCO^+/HOC^+ ratios ranging from 360 to 6000 have been reported depending upon the region of observation.

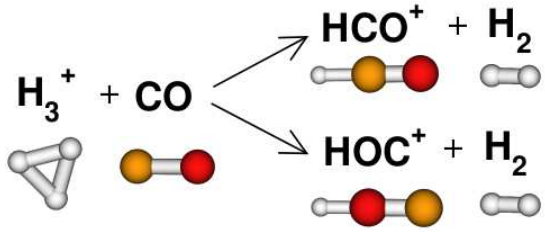

Figure 3.1: H_3^+ + CO Bimolecular Reaction

Several experimental and theoretical investigations of the $[H_3CO]^+$ system probing the structures and energetics, reaction mechanisms, product branching ratios, and $HCO^+ \rightleftharpoons HOC^+$ isomerization have been reported[Illies *et al.*, 1982, 1983; Herbst and Woon, 1996; Chalk and Radom, 1997; Smith *et al.*, 2002; Wester *et al.*, 2002; Moyano *et al.*, 2006; Li *et al.*, 2008; Vogt-Geisse and Toro-Labbé, 2009; Yu, 2009; Klippenstein *et al.*, 2010; Le *et al.*, 2010; Yu, 2011; Carrascosa *et al.*, 2016; Jarrold *et al.*, 1986]. Detailed electronic structure calculations at the benchmark CCSD(T)/CBS level of theory characterizing the potential energy surface and various reaction pathways of the $[H_3CO]^+$ system have been reported[Li *et al.*, 2008]. A weak temperature dependence of the rate constants for the H_3^+ + CO reaction was found in an *ab initio* molecular dynamics study[Yu, 2009]. Further, 26 and 8% of HOC^+ formation was predicted at 298 and 20 K temperatures, respectively, in the same work. Trajectory simulations of H_3^+ + CO collision dynamics on an interpolated analytic PES were performed by Le et al.,[Le *et al.*, 2010]. They reported 40-43% of HOC^+ formation at temperatures of 75-300 K for a range of collision energies.

Klippenstein et al.,[Klippenstein *et al.*, 2010] combined high level electronic structure methods with statistical rate constant calculations and predicted 38 and 19% of HOC^+ formation at T = 300 and 20 K, respectively.

The $HCO^+ \rightleftharpoons HOC^+$ isomerization reaction may influence the observed HCO^+/HOC^+ abundance. Highly accurate electronic structure calculations characterizing the energy profiles of these reactions are available in the literature[Li *et al.*, 2008; Martin *et al.*, 1993; Yamaguchi *et al.*, 1994]. Li et al.,[Li *et al.*, 2008] found that HCO^+ isomer is stable by 37.7 kcal/mol with respect to HOC^+ at the benchmark CCSD(T)/CBS level of theory. Further, they reported 77.1 and 36.9 kcal/mol energy barriers for the forward ($HCO^+ \rightarrow HOC^+$) and backward reactions, respectively. Hence, these reactions require large activation energies. However, in the presence of a catalyst, the barrier for these reactions reduces and even vanishes in the presence of certain molecules such as HF and N_2[Chalk and Radom, 1997; Bohme, 1992]. These studies have shown that the catalyst molecules act as carriers of proton transporting it from C to O end and vice versa. Due to the abundance of hydrogen molecules in space, the H_2 assisted isomerization reaction $H_2 + HOC^+ \rightarrow H_2 + HCO^+$ has been considered as a source of depletion of the isoformyl cation in the interstellar media[Smith *et al.*, 2002; Vogt-Geisse and Toro-Labbé, 2009]. However, smaller rate constants have been reported for this reaction under 100 K temperatures[Herbst and Woon, 1996]. A roaming mechanism for the H_2 catalyzed HOC^+ isomerization reaction has been proposed[Yu, 2011]. Carrascosa et al.,[Carrascosa *et al.*, 2016] have reported a crossed beam velocity map imaging study of the $H_3^+ + CO$ reaction. The dynamics of this reaction was studied for a range of collision energies (E_{rel} =0.2 - 4.3 eV), and the product branching ratios were estimated by fitting a sum of two distribution functions to product internal energy distributions measured in experiments. Less than 10% of HOC^+ formation was predicted at low collision energies, and a maximum of 24% was estimated at $E_{rel} = 1.8$ eV. For E_{rel} greater than 1.8 eV, the measured product internal energies were above the $HCO^+ \rightleftharpoons HOC^+$ isomerization barriers and a distinction between the isomer populations could not be performed. Further, a high degree of product internal energy excitation was observed in the experiments. In the present work, classical chemical dynamics simulations performed for the $H_3^+ + CO$ bimolecular reaction are reported. The simulation conditions were set to mimic the aforementioned crossed beam experiments[Carrascosa *et al.*, 2016].

3.1 METHODOLOGY

The direct dynamics simulations were performed using the density functional PBE0/aug-cc-pVDZ level of electronic structure theory, and this was decided on the basis of the relatively less computational time requirements for density functional theory. Further, stationary point energies on the $[H_3CO]^+$ potential energy surface computed using the chosen level of theory were close to those reported using the benchmark CCSD(T)/CBS method[Li *et al.*, 2008]. For the trajectory initial conditions, normal mode vibrational energies and thermal rotational energies for the H_3^+ molecule were chosen from a 300 K Boltzmann distribution[Peslherbe *et al.*, 1999]. To the diatomic CO molecule, zero point vibrational energy (v = 0) and zero rotational energy were added. The initial center-of-mass separation between H_3^+ and CO molecules was kept at 10.0 Å, and the impact parameter for the collisions was randomly chosen between 0.0 and 4.0 Å. This maximum value was selected on the basis of reactivity observed in trajectories, and it was sufficient for all collision energies except at the lowest value. However, the above-mentioned range of impact parameters was chosen uniformly at all energies. The reactants H_3^+ and CO were randomly oriented in each trajectory. At five different collision energies E_{rel} = 0.2, 0.6, 1.8, 2.7, and 4.3 eV, an ensemble of trajectories was generated. These initial conditions were chosen in accordance with the crossed beam experiments on the $H_3^+ + CO$ reaction by Carrascosa et al.,[Carrascosa *et al.*, 2016] The trajectories were propagated to 2.0 ps or until reaction products were separated by a minimum distance of 12.0 Å. Trajectory integrations were carried out using a sixth order Symplectic integrator[Schlier and Seiter, 1998, 2000] with a step size of 0.5 fs.

3.2 POTENTIAL ENERGY PROFILE

The detailed potential energy profile for the $H_3^+ + CO \rightarrow HCO^+/HOC^+ + H_2$ reaction is presented in Figure 3.2(a) wherein the energies are given in units of kcal/mol without zero point energy corrections. The proton transfer from H_3^+ to CO results in either formyl or isoformyl cation. These reactions are barrier-less and exoergic (due to the low proton affinity of H_2) and proceed via a transition state that lies 4.9 kcal/mol below the reactants. Without zero point energy correction, the $H_2 + HCO^+$ and $H_2 + HOC^+$ products have energies of -40.4 and -0.9 kcal/mol, respectively, with reference to the separated reactants. Reaction pathways incorporate weak product complexes (H_2...HCO^+ and H_2...HOC^+) which dissociate as final products. The formyl cation is stable by 39.5 kcal/mol with respect to the isoformyl cation. The isomerization reaction $HCO^+ \rightarrow HOC^+$ has an energy barrier of 75.4 kcal/mol, and the reverse reaction has a barrier of 35.9 kcal/mol. The energy profile for the $HCO^+ \rightleftharpoons HOC^+$ isomerization reaction is given in Figure 3.2(b). The calculations were performed using the density functional PBE0/aug-cc-pVDZ level of theory. A comparison of the potential energy profiles computed using the PBE0/aug-cc-pVDZ theory and the benchmark CCSD(T)/CBS method[Li *et al.*, 2008] is given in Figure 3.3. Optimized geometries of all stationary points on the $[H_3CO]^+$ potential energy surface are shown in Figure 3.4.

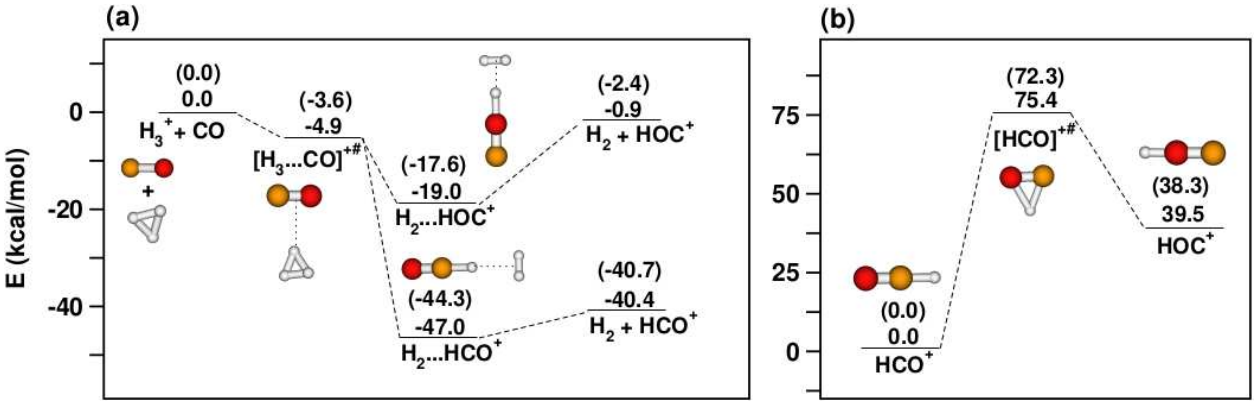

Figure 3.2: Potential energy profiles for (a) the bimolecular reaction $H_3^+ + CO \rightarrow HCO^+/HOC^+ + H_2$ and (b) the $HCO^+ \rightleftharpoons HOC^+$ isomerization reaction. Energies given are in units of kcal/mol and without zero point energy corrections. Also, zero point corrected energies are given in brackets.

3.3 SIMULATION RESULTS

A total of 5000 trajectories (1000 trajectories at a given E_{rel}) were generated. The total energy (E_{tot}) in the trajectories was conserved within $E_{tot} \pm 1.0$ kcal/mol during the integration. Figure 3.5 shows total energy as a function of time for several different classical trajectories. The trajectories were analyzed for reaction mechanisms, branching ratios, energy distributions, and scattering angles.

3.3.1 Reactivity and Branching Ratio

Table 3.1 and Figure 3.6 show a summary of the observed trajectory events. In the table, N is the number of trajectories generated at a given E_{rel}, N_r is the number of reactive trajectories, N_{HCO^+} is the number of trajectories forming $H_2 + HCO^+$, N_{HOC^+} is the number of trajectories forming $H_2 + HOC^+$. The bracketed quantity in column 4 is $(N_{HCO^+}/N_r) \times 100\%$ and the associated error bar. Similarly, $(N_{HOC^+}/N_r) \times 100\%$ and the associated error bar is given in column 5 in brackets. N_{iso} is the number of trajectories showing $HCO^+ \rightleftharpoons HOC^+$ isomerization.

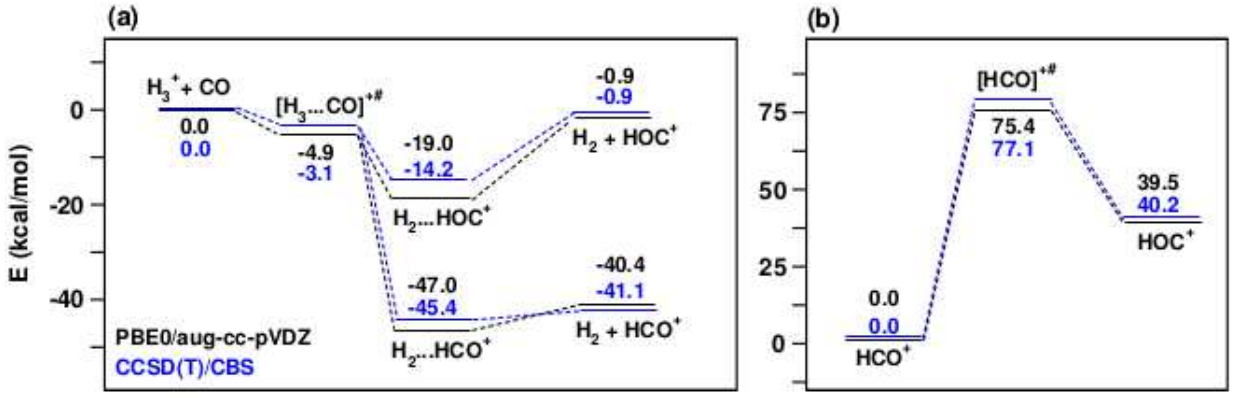

Figure 3.3: Potential energy profiles for (a) the $H_3^+ + CO \rightarrow HCO^+/HOC^+ + H_2$ bimolecular reaction and (b) $HCO^+ \rightleftharpoons HOC^+$ isomerization reaction. Energies are given in units of kcal/mol without zero point energy corrections. Black lines correspond to density functional PBE0/aug-cc-pVDZ theory computed in the present work and blue lines correspond to benchmark CCSD(T)/CBS calculations taken from a previous work[Li *et al.*, 2008].

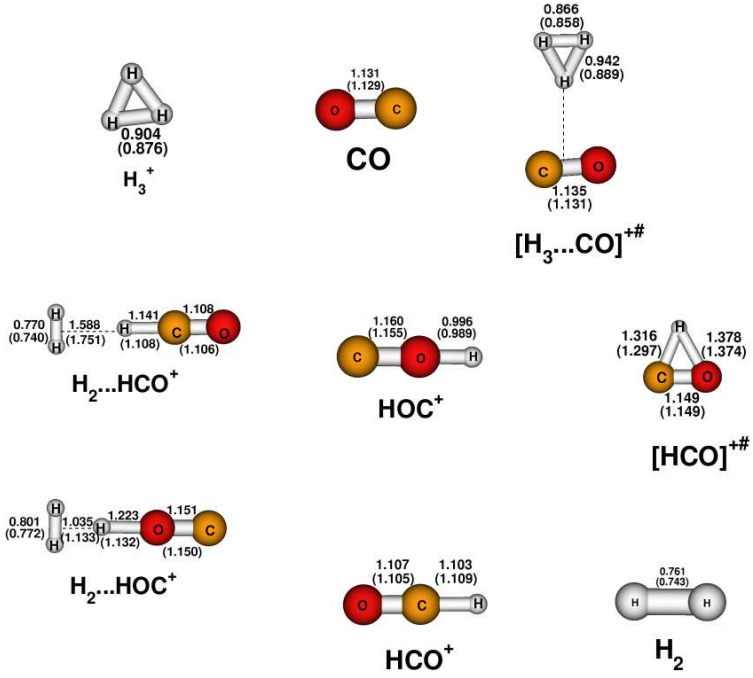

Figure 3.4: Optimized geometries of stationary points on the $[H_3CO]^+$ potential energy surface. The calculations were performed using the density functional PBE0/aug-cc-pVDZ level of theory. The bond lengths are given in units of Å. The numbers in brackets are bond lengths resulting from CCSD(T)/CBS benchmark calculations.

% error shown in Table 3.1 can be calculated by following formula:

$$\%error = \frac{1}{N_o}\sqrt{\frac{N_t(N_o - N_t)}{N_o}} * 100 \tag{3.1}$$

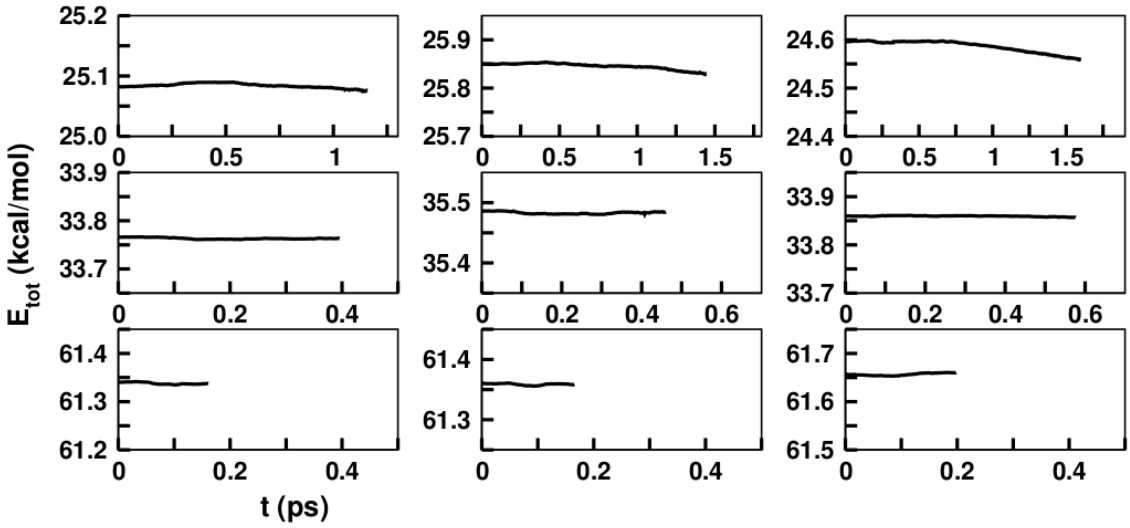

Figure 3.5: Total energy E_{tot} as a function of integration time for several different classical trajectories.

Table 3.1: Summary of Trajectory Events Following H_3^+ + CO Bimolecular Collision Reaction

E_{rel}	N	N_r	N_{HCO^+}	N_{HOC^+}	$\frac{N_{HCO^+}}{N_{HOC^+}}$	N_{iso}
0.2eV	1000	800	527(65.9 ± 1.7%)	273(34.1 ± 1.7%)	1.9	0
0.6eV	1000	561	425(75.8 ± 1.8%)	136(24.2 ± 1.8%)	3.1	0
1.8eV	1000	318	228(71.7 ± 2.5%)	90(28.3 ± 2.5%)	2.5	1
2.7eV	1000	250	184(73.6 ± 2.8%)	66(26.4 ± 2.8%)	2.8	4
4.3eV	1000	191	135(70.7 ± 3.3%)	56(29.3 ± 3.3%)	2.4	19

In equation 3.1, N_o is number of total reactive trajectories at given E_{rel} and N_t is number of trajectories of HCO^+ or HOC^+ at given E_{rel}.
The overall reactivity was dependent on the collision energy and decreased with an increase in E_{rel}. The H_3^+ + CO reaction is barrier-less and exoergic and does not need activation. At the lowest E_{rel} (0.2 eV), 80.0% of the trajectories were reactive, and at the highest E_{rel} (4.3 eV), reaction occurred only in 19.1% of the trajectories. At high E_{rel} values, the reactants do not spend a sufficient amount of time in close proximity for the proton transfer to take place–they fly off of each other (except at very low impact parameters). Reactivity enhances at low collision energies, as seen from Figure 3.6. The reactive trajectories were classified as either HCO^+ or HOC^+ trajectory (listed as N_{HCO^+} and N_{HOC^+} in Table 3.1) depending upon which isomer resulted upon collision. The subsequent $HCO^+ \rightleftharpoons HOC^+$ auto-isomerization, if it happened in a trajectory, was ignored while classifying the trajectory. Only at the highest collision energy, an appreciable fraction of trajectories (≈10%) showed isomerization. The high energy HOC^+ isomer resulted in a lesser number of trajectories in comparison to the HCO^+ isomer. For E_{rel} = 0.2, 0.6, 1.8, 2.7, and 4.3 eV, the computed branching ratios (N_{HCO^+}/N_{HOC^+}) were 1.9, 3.1, 2.5, 2.8, and 2.4, respectively. At all energies, HCO^+ dominated over HOC^+ and the branching ratios did not show any particular trend with E_{rel}.

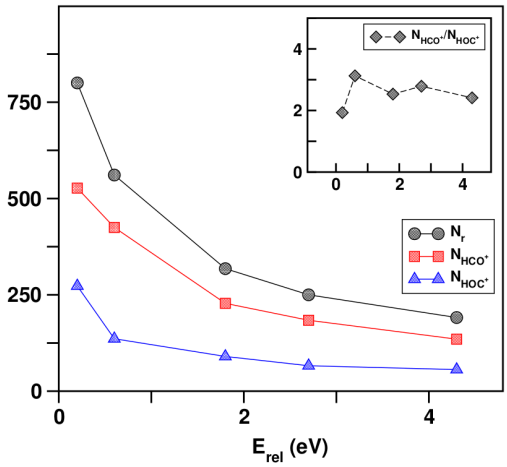

Figure 3.6: Number of reactive trajectories (black circles), trajectories resulting in $HCO^+ + H_2$ (red squares), and $HOC^+ + H_2$ (blue triangles) as a function of relative energy E_{rel}. The inset (black diamonds) shows branching ratios between HCO^+ and HOC^+ products as a function of E_{rel}.

3.3.2 Product Energy Distributions

From the trajectories, vibrational (E_{vib}) and rotational (E_{rot}) energies of the reaction products were computed by two different methods. In the first method, all of the reactive trajectories were included while calculating the product energies without using any zero point energy (ZPE) constraint. In the second, only those trajectories satisfying a soft ZPE constraint[Czakó *et al.*, 2013; Czakó, 2013] were used. According to this constraint, trajectories in which the sum of product vibrational energies was greater than the total zero point energies of the products were to be considered. The total ZPEs of $HCO^+ + H_2$ and $HOC^+ + H_2$ products are 0.66 and 0.61 eV, respectively. Internal energy E_{int} ($=E_{vib} + E_{rot}$) distributions of the HCO^+ and HOC^+ isomers are presented in Figure 3.7. The first row shows E_{int} distributions of HCO^+ and HOC^+ products computed using all of the reactive trajectories. The second row presents similar data computed from those trajectories which satisfied the ZPE constraint. In the third row, normalized and ZPE constrained energy distributions are shown for only the HCO^+ isomer, and the fourth row shows similar data for HOC^+. Each column corresponds to a given E_{rel}. Energy distributions without the ZPE constraint (first row) are presented for comparison only, and for discussion purposes, the ZPE constrained data are used. Internal energy distributions shown in Figure 3.7 agree qualitatively with the experimental distributions[Carrascosa *et al.*, 2016]. Energy distributions from the simulations are peaked at slightly lower values in comparison to the corresponding experimental data. Nonetheless, simulations indicate a high degree of internal excitation in agreement with the experimental work. Such high internal energy transfers were observed in a few other proton transfer reactions also[Carrascosa *et al.*, 2015; Suits, 2008]. Energy distributions of HCO^+ and HOC^+ products shown in the second row of Figure 3.7 are essentially monomodal, in agreement with experiments. It was proposed in the experimental work[Carrascosa *et al.*, 2016] that the monomodal distribution was a result of overlapping energy distributions of HCO^+ and HOC^+ isomers. One can observe from Figure 3.7 that the individual isomer energy distributions (shown in the third and fourth rows) when combined and normalized result in the observed monomodal energy distributions. The experimentally observed width of the E_{int} distributions was ascribed to the intrinsic reaction dynamics, i.e., varying energy partitioning among the degrees of freedom of the reaction products for different collision events rather than experimental factors such as the uncertainty in E_{rel}. This prediction also agrees with the present calculations. Clearly, the spread observed in the experimental plots is also seen in the simulation results presented in Figure 3.7.

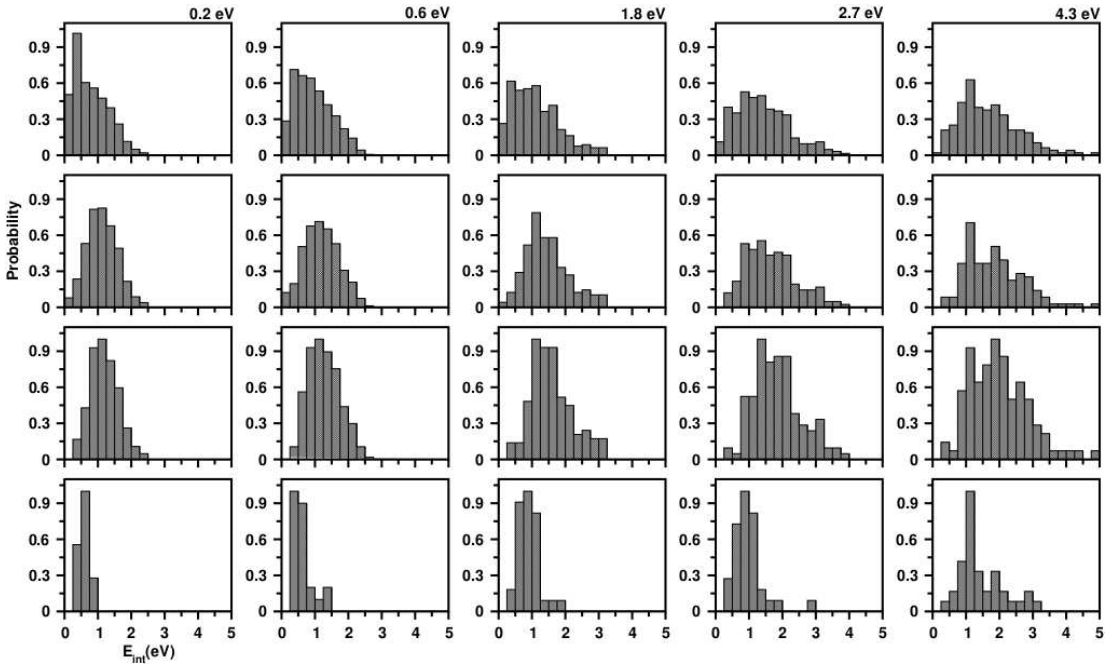

Figure 3.7: First row (from the top): normalized internal energy ($E_{int} = E_{vib} + E_{rot}$) distributions of HCO^+ and HOC^+ products computed using all of the reactive trajectories. Second row: normalized E_{int} distributions from only those trajectories satisfying the soft ZPE constraint. Third row: normalized and ZPE constrained E_{int} distributions for only HCO^+ isomer. Fourth row: similar data for only HOC^+ isomer. The x-axes ranges are identical in all of the plots, and E_{rel} is fixed for a given column.

This spread increases with an increase in E_{rel} and is a result of multiple pathways by which the available energy was distributed among the translational, vibrational, and rotational degrees of freedom of the reaction products.

A qualitative understanding about which rovibrational modes of the reaction products are excited can be achieved by analyzing the E_{rot} and E_{vib} of both ionic (HCO^+ and HOC^+) and neutral (H_2) products. Trajectory averaged E_{int}, E_{rot}, and E_{vib} of the HCO^+ and HOC^+ isomers are presented in parts a and b of Figure 3.8, respectively. The insets in these figures show similar data for the associated H_2 product. Clearly, internal energy transfer is substantial for the ionic products and minimum for the neutral product H_2 irrespective of E_{rel}. Further, HCO^+ and HOC^+ are vibrationally more excited than the rotational degrees of freedom. Specifically, the bending modes were excited, as observed from visualization of the trajectories. The fraction of energy transfer to the rovibrational degrees of freedom of HCO^+ and HOC^+ was computed from the trajectories. The quantity f_{int} defined as the trajectory averaged ratio of E_{int} of HCO^+ and HOC^+ and the available (kinetic) energy is plotted in Figure 3.8c as a function of E_{rel}.
f_{int} can be represented by following formula:

$$f_{int} = \frac{E_{int}}{E_{kinetic}} \tag{3.2}$$

This figure can be compared directly with the experimental data given in Figure 2 of Carrascosa et al.,[Carrascosa *et al.*, 2016]. Though the fractions computed from the simulations are slightly lower in comparison to experiments, the qualitative behavior remains the same i.e., f_{int} decreases slowly with an increase in collision energy. Further, the quantity f_{int} was computed for specific ranges of product scattering angles θ and plotted in Figure 3.8c (a discussion about product scattering angle distributions is given in the next section). In Figure 3.8c, red squares, green squares, and blue diamonds correspond to the θ ranges (0–20°), (30–50°), and (60–80°), respectively. Clearly,

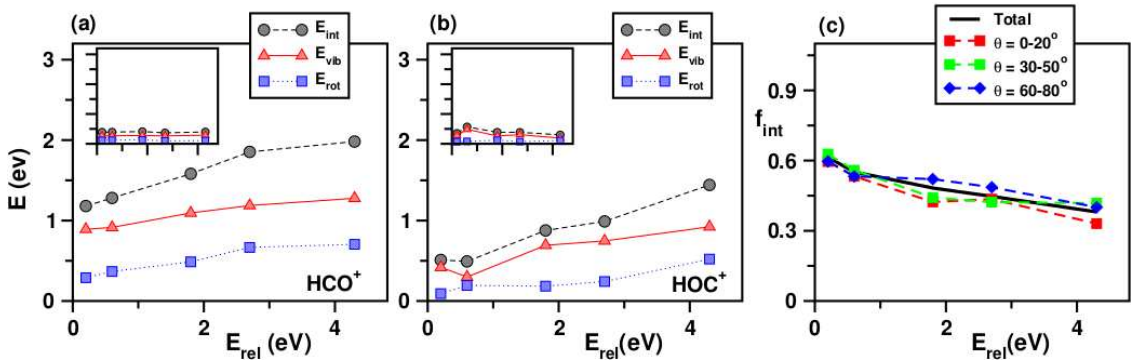

Figure 3.8: (a)Trajectory averaged HCO^+ rotational energy (E_{rot}, blue squares), vibrational energy (E_{vib}, red triangles), and internal energy (E_{int}, black circles) plotted as a function of E_{rel}. (b) Similar data but for HOC^+. The insets in part a and b show similar data for H_2. (c) Trajectory averaged fraction (f_{int}) of total energy being transferred as internal energy to the ionic reaction products (HCO^+ and HOC^+) is plotted as a function of E_{rel}. The quantity f_{int} is given for all scattering angles θ (black), trajectories with θ = 0–20° (red), θ = 30–50° (green), and θ = 60–80°(blue).

the trend of the decrease in f_{int} with E_{rel} remains nearly the same for different ranges of scattering angles in agreement with experiments[Carrascosa *et al.*, 2016], which indicates that the internal energy transfer is independent of scattering angle. As discussed in the next section, the scattering angle distributions computed from the trajectories showed that forward scattering was dominant at all E_{rel} except at the lowest value at which the distribution had a forward–backward symmetry. The quantity f_{int} from trajectories undergoing backward scattering ($\theta > 90°$) was computed and it is almost the same as f_{int} estimated from forward scattering trajectories for E_{rel} = 0.2 eV.

3.3.3 Scattering Angles

The product scattering angles θ and their distributions $P(\theta)$ were computed from the trajectories. The definition of θ (shown in Figure 3.9) is such that small values of θ indicate forward scattering (in the direction of incoming CO molecule) and large values indicate backward scattering. Figure 3.9 shows normalized scattering angle distributions computed from HCO^+ trajectories, HOC^+ trajectories, and all of the reactive trajectories in the first, second, and third columns, respectively. Each row corresponds to a given E_{rel}. In general, forward scattering was dominant except at the lowest E_{rel} (first row) wherein an approximate forward–backward symmetry can be observed. With an increase in collision energy, forward scattering becomes dominant (in agreement with experiments[Carrascosa *et al.*, 2016]) with a major fraction of trajectories having $\theta \leq 30°$. These fractions are 15 ± 1.3, 32 ± 1.9, 39 ± 2.7, 46 ± 3.2, and 36 ± 3.5% at E_{rel} = 0.2, 0.6, 1.8, 2.7, and 4.3 eV, respectively. These small θ values indicate a stripping type of mechanism by which the CO abstracts a proton from the H_3^+ molecule. This was verified by visual inspection of the trajectories.

3.4 DISCUSSION

Carrascosa et al.,[Carrascosa *et al.*, 2016] carried out crossed beam velocity map imaging experiments on the $H_3^+ + CO \rightarrow HCO^+/HOC^+ + H_2$ reaction and predicted product ratios by fitting a sum of two distribution functions to the measured E_{int} distributions. It was assumed that the relative energy loss for both of the isomer channels is the same in this fitting procedure. They

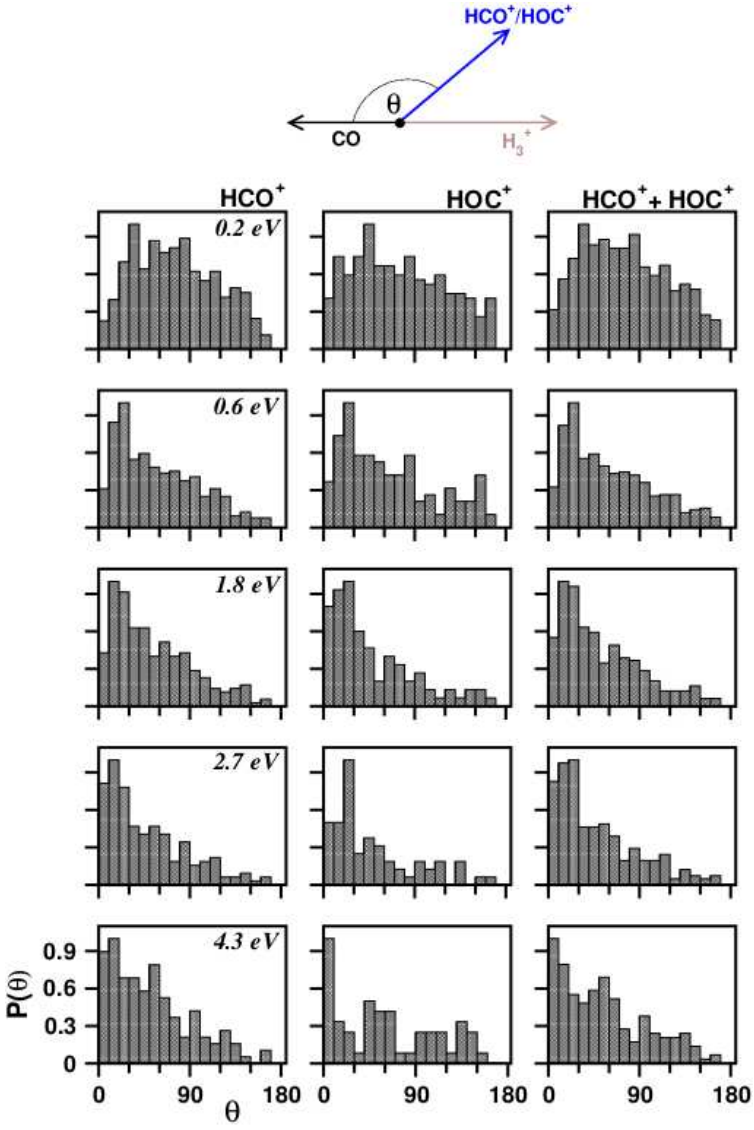

Figure 3.9: Normalized product scattering angle distributions computed from HCO^+ trajectories, HOC^+ trajectories, and total reactive trajectories shown in the first, second, and third columns, respectively. E_{rel} is the same in a given row. Respective axes ranges are the same in all of the plots.

Table 3.2: Relative Energy Loss for the Two Isomer Channels

E_{rel}	$\frac{\langle E_{int}^{HCO^+} \rangle}{E_{max}^{HCO^+}}$	$\frac{\langle E_{int}^{HOC^+} \rangle}{E_{max}^{HOC^+}}$
0.2eV	0.605	2.116
0.6eV	0.545	0.768
1.8eV	0.445	0.476
2.7eV	0.416	0.361
4.3eV	0.328	0.332

estimated a maximum of 24% of HOC^+ formation at E_{rel} = 1.8 eV and less than 10% at the two lower E_{rel} values. The fitting was not done at higher collision energies, as the reaction products had E_{int} greater than the isomerization barriers and a distinction between the two isomers was not possible[Carrascosa *et al.*, 2016]. In the present simulations, 34.1, 24.2, 28.3, 26.4, and 29.3% of HOC^+ formation was observed at E_{rel} = 0.2, 0.6, 1.8, 2.7, and 4.3 eV, respectively (Table 3.1). Larger fractions of the high energy HOC^+ isomer formation at low E_{rel} were observed in simulations in contrast to experimental predictions. Such high fractions of HOC^+ have been reported in previous theoretical studies. Le et al.,[Le *et al.*, 2010] predicted 40-43% of HOC^+ in a classical trajectory study of the H_3^+ + CO reaction on an interpolated potential energy surface. This study was performed at temperatures of 75–300 K and with relative collision energies below 0.2 eV. Further, 26% of HOC^+ was predicted[Yu, 2009] in an *ab initio* molecular dynamics study performed at 298 K temperature and 38% was reported by Klippenstein et al.,[Klippenstein *et al.*, 2010] based on electronic structure theory and statistical rate constant calculations. To investigate further this discrepancy between the experimental and computed branching ratios at low E_{rel} values, the assumption used in the fitting procedure in the experimental work[Carrascosa *et al.*, 2016] was tested in the present work. It was assumed in the experimental study that the relative energy loss for the two isomer channels is the same, i.e., $\langle E_{int}^{HCO^+} \rangle / E_{max}^{HCO^+} = \langle E_{int}^{HOC^+} \rangle / E_{max}^{HOC^+}$, where $\langle E_{int}^{HCO^+} \rangle$ and $\langle E_{int}^{HOC^+} \rangle$ are average internal energies taken from Figure 3.8 and $E_{max}^{HCO^+} = E_{rel}$ –(–1.75eV) and $E_{max}^{HOC^+} = E_{rel}$ –(–0.04eV). Here, –1.75 and –0.04 eV are the exoergicities of the HCO^+ and HOC^+ isomer formation pathways, respectively. Results of these calculations are summarized in Table 3.2 which shows that the assumption may not be valid at low collision energies. With an increase in E_{rel}, the relative energy losses for both of the isomer channels are becoming roughly equivalent. At E_{rel} = 1.8 eV, simulations show 28.3% of HOC^+, while the experimental prediction is 24.0%. It is possible that the branching ratios found from simulations and experiment might be similar at the high collision energies (2.7 and 4.3 eV) though branching ratios were not reported in the experiment for these energies.

Scattering angle distributions shown in Figure 3.9 indicate primarily forward scattering at all collision energies except at the lowest energy E_{rel} = 0.2 eV. Snapshots of a typical trajectory showing forward scattering are shown in Figure 3.10a, which lead to $HCO^+ + H_2$ products via proton transfer at ≈ 82 fs. E_{rel} = 2.7 eV for this trajectory, and the product scattering angle was 26.62°. At large collision energies, $HCO^+ \rightleftharpoons HOC^+$ isomerization (without catalytic assistance) took place and 1, 4, and 19 trajectories showed isomerization at E_{rel} = 1.8, 2.7, and 4.3 eV, respectively. Snapshots of example trajectories are shown in Figure 3.10b, c, and d. In Figures 3.10b and c, $HCO^+ \rightleftharpoons HOC^+$ isomerization can be observed via bending transition state in the frames 105 fs and 110 fs, respectively, and results in $HCO^+ + H_2$ and $HOC^+ + H_2$ formation at E_{rel} = 4.3 eV. In Figure 3.10d, $HCO^+ \rightarrow HOC^+$ isomerization can be observed in the 145 fs frame. These isomerization reactions did not affect the product branching ratios significantly, and the uncatalyzed $HCO^+ \rightleftharpoons HOC^+$ isomerizations may not be that important in the interstellar conditions[Larsson *et al.*, 2012].

The forward-backward symmetry observed in the θ distribution at the lowest E_{rel} can be attributed to the variety of dynamical behavior observed at this energy. Out of the 800 total reactive trajectories, 21% of them (171/800) showed formation of H_2...HCO^+ and H_2...HOC^+ product complexes. The lifetime for these complexes varied between a few vibrational periods to a few hundred femtoseconds, and during this time, they underwent rotations, thus resulting in large scattering angles. Snapshots of an example trajectory are presented in Figure 3.10e along with relevant bond distances. In this trajectory, the H_2...HOC^+ complex resulted at ≈270 fs and had a lifetime of ≈330 fs, which is indicated by a red line in the plot of O-H2 bond distance. The scattering angle for this trajectory was 118.07°. Another interesting feature was observed in 35 out of 527 HCO^+ trajectories at E_{rel} = 0.2 eV. In these, H_3^+ approached the O end of CO and proton transfer occurred, resulting in HOC^+. Subsequently, the proton jumped back to H_2, resulting in H_3^+ which then transferred the proton to C, resulting in HCO^+. In many of these trajectories, the H_3^+ (after the proton hopping) moved around CO at larger distances, indicating the operation of a possible roaming mechanism[Suits, 2008]. Snapshots of an example trajectory showing this behavior are given in Figure 3.10f along with appropriate bond coordinates. In this trajectory, the HOC^+ formed at 220 fs, but the proton immediately bounced back to H_2. The resulting H_3^+ moved around CO (for ≈400 fs), and then, proton transfer occurred to C, resulting in HCO^+.

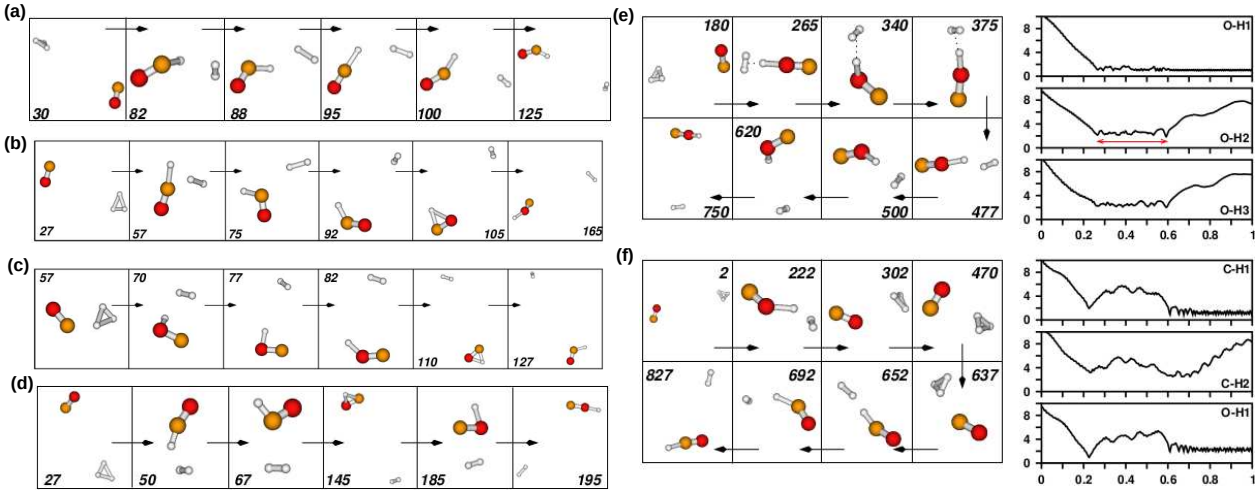

Figure 3.10: Snapshots of trajectories (a) showing forward scattering at E_{rel} = 2.7 eV, (b),(c), and (d) showing isomerization at E_{rel} = 4.3 eV, (e) forming a H_2...HOC^+ complex before dissociation at E_{rel} = 0.2 eV, (f) forming HOC^+ initially and then resulting in HCO^+ via a roaming mechanism at E_{rel} = 0.2 eV. Relevant bond distances (in Å) as a function of time (in ps) are given in parts e and f. The number given inside each frame is the time (in fs) at which the snapshot was taken.

Snapshots of more trajectories showing different kinds of behavior are presented in Figure 3.11 at E_{rel} = 0.2 eV. Figure 3.11a shows HCO^+ + H_2 product formation via the H_2...HCO^+ complex. The complex has a lifetime of ≈80 fs (between 190 to 270 fs). Figure 3.11b results in HCO^+ + H_2 via formation of H_2...HCO^+ complex. The complex has a lifetime of ≈170 fs (between 190 to 360 fs). Figure 3.11c results in HOC^+ + H_2 and then proton hops back resulting in H_3^+ + CO. The H_3^+ roams around CO and then transfers the proton to C resulting in HCO^+ + H_2. Figure 3.11d shows formation of HOC^+ + H_2 and then proton hops back resulting in H_3^+ + CO. The H_3^+ roams around CO and then transfers the proton to C resulting in HCO^+ + H_2. Figure 3.11e shows formation of HOC^+ + H_2 and then proton hops back resulting in H_3^+ + CO. The H_3^+ roams around CO and then transfers the proton to O resulting in HOC^+ + H_2. Figure 3.11f shows formation of HCO^+ + H_2 via H_2...HOC^+ complex. The complex has a lifetime of ≈380 fs (between 210 to 590 fs).

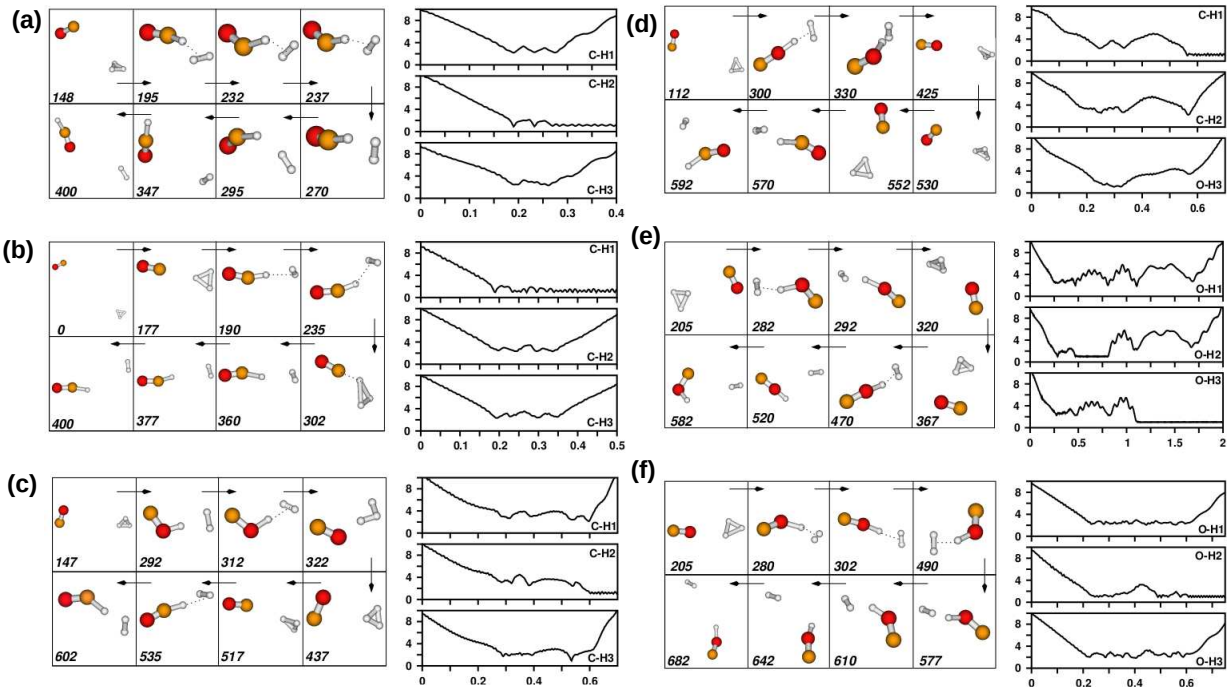

Figure 3.11: Snapshots and relevant bond distances of example trajectories showing different dynamical behavior at E_{rel} = 0.2 eV. Relevant bond distances (in Å) are given as a function of time (in ps). The number given inside each frame is the time (in fs) at which the snapshot was taken.

Roaming in the H_3^+ + CO system has been reported previously in the literature[Yu, 2011], and roaming was observed in 30 out of the total 800 reactive trajectories at E_{rel} = 0.2 eV involving the motion of H_3^+. In another seven trajectories at the same collision energy, a roaming mechanism involving H_2 was observed. In these trajectories, H_3^+ + CO collision led to HCO^+/HOC^+ + H_2 and then H_2 moved around the ionic product instead of leaving and abstracted the proton and transferred again to CO (resulting in the same or different isomer). This H_2 influenced isomerization happened in less than seven trajectories, which is in agreement with a previous study[Klippenstein *et al.*, 2010] that the H_2 catalyzed isomerization (H_2 + $HCO^+ \rightleftharpoons H_2$ + HOC^+) may not be that efficient. The variety of dynamical behavior discussed above was important only at E_{rel} = 0.2 eV. Roaming and complex formations were observed in only a negligible number of trajectories at E_{rel} = 0.6 eV, and no such behaviors were observed at higher energies. Low collision energies and the existence of product complexes have been considered as factors responsible for the roaming mechanism[Yu, 2011].

3.5 SUMMARY

Direct chemical dynamics simulations were reported for the H_3^+ + CO bimolecular reaction for a range of collision energies. This is one of the important reactions occurring in the interstellar media, and the simulations were performed to model a recently reported velocity map imaging study[Carrascosa *et al.*, 2016]. The product isomer ratios obtained from the present simulations at low collision energies are in contrast with the experimental predictions but are in agreement with previous theoretical studies[Yu, 2009; Klippenstein *et al.*, 2010; Le *et al.*, 2010]. Internal energy and scattering angle distributions are in qualitative agreement with the experimental work. Scattering angle distributions were peaked at low values, indicating primarily forward scattering at all energies except for the lowest E_{rel}. This pointed toward the operation of a stripping type mechanism which

was verified by visualization of the trajectories. At the lowest E_{rel}, interesting dynamical features including a roaming mechanism were observed which lead to the broad scattering angle distribution. The $HCO^+ \rightleftharpoons HOC^+$ isomerization was observed in a small fraction of trajectories at high collision energies but did not play a significant role in determining the branching ratios. It is important to note that the reaction considered here is a proton transfer reaction which implies quantum effects might be playing a role in determining the rate constants and branching ratios. In the present work, the CO molecule had zero rotational angular momentum and zero point vibrational energy. The effects of vibrational/rotational excitation of CO on the product branching ratios will be an interesting future work.